ENVIRONMENTAL RESEARCH
LETTERS

LETTER • OPEN ACCESS

Assessing terrestrial biogeochemical feedbacks in a strategically geoengineered climate

To cite this article: Cheng-En Yang *et al* 2020 *Environ. Res. Lett.* **15** 104043

View the article online for updates and enhancements.

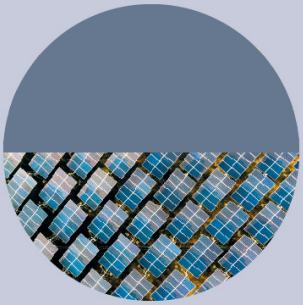

ENVIRONMENTAL RESEARCH
INFRASTRUCTURE AND SUSTAINABILITY™

No publication charges until 2021. Submit your research **iopscience.org/eris**

Editor-in-Chief
Arpad Horvath, University of California, Berkeley, USA

This content was downloaded from IP address 73.108.195.248 on 14/12/2020 at 23:24

Environmental Research Letters

LETTER

Assessing terrestrial biogeochemical feedbacks in a strategically geoengineered climate

Cheng-En Yang[1,2], Forrest M Hoffman[1,2], Daniel M Ricciuto[3], Simone Tilmes[4,5], Lili Xia[6], Douglas G MacMartin[7], Ben Kravitz[8,9], Jadwiga H Richter[5], Michael Mills[4] and Joshua S Fu[1,2]

[1] Department of Civil and Environmental Engineering, University of Tennessee, Knoxville, TN 37996, United States of America
[2] Climate Change Science Institute and Computational Sciences and Engineering Division, Oak Ridge National Laboratory, Oak Ridge, TN 37831, United States of America
[3] Climate Change Science Institute and Environmental Sciences Division, Oak Ridge National Laboratory, Oak Ridge, TN 37831, United States of America
[4] Atmospheric Chemistry, Observations, and Modeling Laboratory, National Center for Atmospheric Research, Boulder, CO 80307, United States of America
[5] Climate and Global Dynamics Laboratory, National Center for Atmospheric Research, Boulder, CO 80307, United States of America
[6] Department of Environmental Sciences, Rutgers University, New Brunswick, NJ 08901, United States of America
[7] Sibley School of Mechanical and Aerospace Engineering, Cornell University, Ithaca, NY 14853, United States of America
[8] Department of Earth and Atmospheric Sciences, Indiana University, Bloomington, IN 47405, United States of America
[9] Atmospheric Sciences and Global Change Division, Pacific Northwest National Laboratory, Richland, WA 99352, United States of America

E-mail: forrest@climatemodeling.org

Keywords: geoengineering, carbon cycle, terrestrial biogeochemical feedbacks

Supplementary material for this article is available online

OPEN ACCESS

RECEIVED
12 February 2020

REVISED
6 July 2020

ACCEPTED FOR PUBLICATION
6 August 2020

PUBLISHED
28 September 2020

Original content from this work may be used under the terms of the Creative Commons Attribution 4.0 licence.

Any further distribution of this work must maintain attribution to the author(s) and the title of the work, journal citation and DOI.

Abstract

Geoengineering by injecting sulfur dioxide (SO_2) into the lower stratosphere has been suggested to reduce anthropogenically induced warming. While impacts of such geoengineering on climate have been investigated in recent decades, few modeling studies have considered biogeochemical feedbacks resulting from such intervention. This study comprehensively characterizes responses and feedbacks of terrestrial ecosystems, from an ensemble of coupled high-resolution Earth system model climate change simulations, under the highest standard greenhouse gas scenario with an extreme geoengineering mitigation strategy. Under this strategy, temperature increases beyond 2020 levels due to elevated anthropogenic carbon dioxide (CO_2) were completely offset by the SO_2 injection. Carbon cycle feedbacks can alter the trajectory of atmospheric CO_2 levels by storing or releasing additional carbon on land and in the ocean, thus moderating or amplifying climate change. We assess terrestrial biogeochemical feedbacks to climate in response to geoengineering, using model output from the Stratospheric Aerosol Geoengineering Large Ensemble (GLENS) project. Results indicate terrestrial ecosystems become a stronger carbon sink globally because of lower ecosystem respiration and diminished disturbance effects under geoengineering. An additional 79 Pg C would be stored on land by the end of the twenty-first century, yielding as much as a 4% reduction in atmospheric CO_2 mole fraction without marine biogeochemical feedbacks, compared to the high greenhouse gas scenario without geoengineering.

1. Introduction

Rising global mean surface temperature along with increasing anthropogenic greenhouse gas emissions have been observed since the last century (IPCC 2014), and future projections of increasing global mean surface temperature remain even if anthropogenic emissions are reduced (Steffen *et al* 2018). To prevent continued warming that could cause devastating damage to natural ecosystems and human socio-economic activities (Hoegh-Guldberg *et al* 2018), various climate intervention strategies, such as solar radiation management (SRM), have been proposed to offset the risks of warming (Crutzen 2006, Shepherd 2009). SRM includes various techniques—surface albedo approaches (e.g. brightening of human

© 2020 The Author(s). Published by IOP Publishing Ltd

settlements), cloud-albedo enhancement (e.g. marine cloud brightening), stratospheric aerosols (e.g. sulfate aerosols oxidized from gaseous hydrogen sulfide or SO_2), and space-based techniques (e.g. space reflectors placed in low Earth orbit)—that reduce incoming solar radiation by intentionally increasing Earth's surface albedo (Shepherd 2009). Among the SRM techniques, stratospheric aerosol proposals draw attention widely because of their relatively low cost for mitigating the surface temperature warming and their evenly-distributed cooling capability around the world (Solar Radiation Management Governance Initiative 2011). Inspired by the surface cooling effects of large volcanic eruptions that expel gases into the stratosphere (Robock 2000), most stratospheric aerosol research in past decades focused on stratospheric SO_2 injections (e.g. Robock *et al* 2008, Kravitz *et al* 2013, Tjiputra *et al* 2016, Xia *et al* 2016, Tilmes *et al* 2018) since the gas can be released by large volcanic eruptions into the stratosphere and react to form sulphate aerosols, which can be circulated through the stratospheric winds and dim the incoming insolation. Extensive analyses of Earth System Model (ESM) simulations have addressed climate impacts of stratospheric SO_2 injection, including stratospheric ozone depletion (Tilmes *et al* 2008), weakening of monsoons (Robock *et al* 2008, Tilmes *et al* 2013), acid deposition and ocean acidification (Kravitz *et al* 2009, Moreno-Cruz and Keith 2013), repartitioning of direct and diffuse radiation (Gu *et al* 2003, Mercado *et al* 2009), and suppressed precipitation (Bala *et al* 2008). Terrestrial biogeochemical (BGC) responses have received limited attention in such simulations, particularly for optimized aerosol injection strategies or for high greenhouse gas forcing scenarios using fully coupled ESMs (Keller *et al* 2014, Tjiputra *et al* 2016, Xia *et al* 2016, Cao and Jiang 2017, Keith *et al* 2017, Dagon and Schrag 2019, Duan *et al* 2020).

A recent geoengineering modeling activity known as the Stratospheric Aerosol Geoengineering Large Ensemble (GLENS) project (Tilmes *et al* 2018) simulated the climate response to stratospheric SO_2 injections designed to maintain three temperature goals at their 2020 levels, under the Representative Concentration Pathway 8.5 (RCP8.5) emission scenario (Riahi *et al* 2011): (1) the global mean surface temperature, (2) the interhemispheric surface temperature gradient, and (3) the equator-to-pole surface temperature gradient. The simulations were conducted with the Community Earth System Model (CESM) version 1 with the Whole Atmosphere Community Climate Model (WACCM) as its atmospheric component (Mills *et al* 2017), the Community Land Model version 4.5 with prescribed time-evolving distributions of vegetation consistent with RCP8.5 and interactive carbon and nitrogen cycles as the land component (Oleson *et al* 2013), the Los Alamos Sea Ice Model (Community Ice CodE version 4) as the sea ice component (Hunke and Lipscomb 2008), and the Parallel Ocean Program version 2 as the ocean component (Danabasoglu *et al* 2012). SO_2 was injected in the lower stratosphere at optimized locations to achieve the three temperature goals (Kravitz *et al* 2017) from 2020 to 2099 and to avoid overcooling of the tropics and undercooling of the poles that lead to continued Arctic summer sea ice loss (Moore *et al* 2014, Tilmes *et al* 2016). The large number of ensemble members, a longer simulation period, higher model grid resolutions, effects of sulfate aerosols on stratospheric chemistry, and a high anthropogenic emission scenario through the coupled CESM simulations enable GLENS to serve the needs of a more comprehensive examination of geoengineering impacts, including effects on atmospheric chemistry and land biogeochemical feedbacks to the Earth system. While the fully coupled GLENS simulation results have been used to investigate a wide variety of physical climate responses to aerosol geoengineering (e.g. Tilmes *et al* 2018, Fasullo *et al* 2018, Cheng *et al* 2019), the responses and feedbacks of terrestrial ecosystems to this geoengineered climate have not been evaluated. This study complements those as the first to comprehensively characterize the responses and feedbacks of terrestrial ecosystems to rapidly rising CO_2 levels, producing strong CO_2 fertilization responses, without significant changes in global mean surface temperature or consequent warming-induced changes in precipitation after 2020. Our results not only quantify the terrestrial BGC feedbacks in GLENS but also illustrate the importance of terrestrial ecosystems on future climate change in a strategically geoengineered climate.

2. Data and methods

2.1. Stratospheric aerosol geoengineering large ensemble (GLENS) dataset

GLENS has large ensemble member outputs from two experiments. The baseline experiment consists of a 20-member ensemble of simulations from 2010 to 2099 under the RCP8.5 emission scenario (Riahi *et al* 2011) used in the Fifth Phase of the Coupled Modeling Intercomparison Project (CMIP5), with the first three ensembles simulated at least until the year 2097. Each member started from the same ocean state and differed by small perturbations to their initial atmospheric states. The geoengineering experiment followed the same design as the baseline experiment except for optimized SO_2 injections along 180°E at 30°N, 15°N, 15°S, and 30°S in the lower stratosphere (25 km for 15° and 22.8 km for 30°) (Kravitz *et al* 2017) starting at year 2020. The SO_2 injection rate was adjusted annually during 2020–2099, using a feedback algorithm that maintained global mean surface temperature, the interhemispheric surface temperature gradient, and the equator-to-pole surface temperature gradient at their 2020 levels (Macmartin

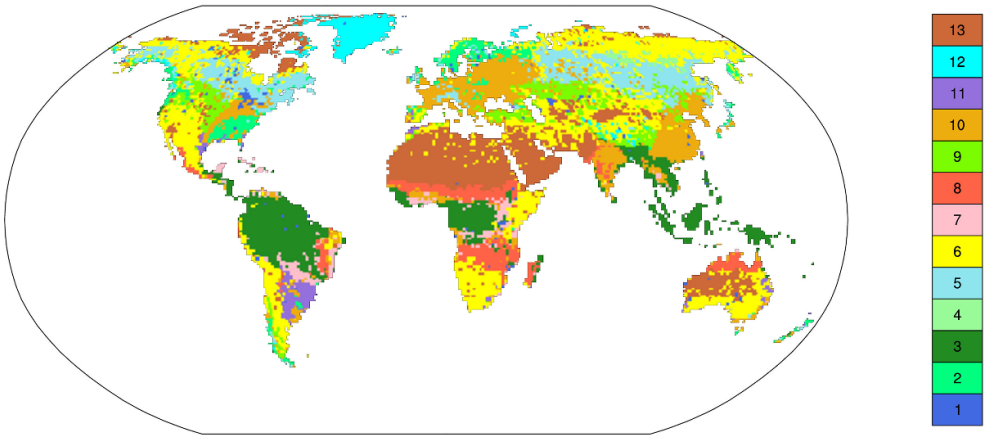

Figure 1. Ecoregions defined in this study.

et al 2014, Kravitz *et al* 2016, 2017). Because only the first three (of 20) ensemble members in the baseline experiment were extended to at least year 2097, the first three ensemble members from the baseline experiment during 2010–2019 (called '*BASE*' hereafter) and during 2020–2097 (called '*CTRL*' hereafter), and the first three ensemble members from the geoengineering experiment during 2020–2097 (called '*GEOENG*' hereafter) are analyzed to fairly compare the differences in climate and terrestrial biogeochemical feedbacks between the baseline and geoengineering experiments, as well as those differences with respect to the present climate. In this study, we apply the two-tailed Student's *t*-test to evaluate if changes between two experiments are significant ($p < 0.1$). In performing the *t*-test, we properly adjusted for lag-one autocorrelation by computing an equivalent sample size that effectively decreases the number of degrees of freedom in determining the standard error of the mean for each of the time series (see supplementary information section 2 for details (available online at stacks.iop.org/ERL/15/104043/mmedia)). Reported correlation coefficients for two variables from spatial maps of differences between experiments are evaluated using the linear Pearson's correlation without removing the global mean (called uncentered), following the method described in IPCC (2001).

2.2. Ecoregions

We define 13 ecoregions in this study by clustering climate, soil, and topography information into regions that were fitted to the International Geosphere-Biosphere Programme (IGBP) ecoregion definitions (Townshend 1992, Hargrove and Hoffman 2004, Hargrove *et al* 2006) (figure 1). The terrestrial BGC feedbacks and responses of ecosystems to the climate with and without geoengineering are compared globally as well as over individual ecoregions.

2.3. Adjusted trajectories of atmospheric CO_2 and surface temperatures

The carbon budget in the terrestrial ecosystem can be expressed, according to the Intergovernmental Panel on Climate Change (Watson *et al* 2000) as

$$\begin{aligned} GPP &= NPP + R_a = NEP + R_h + R_a \\ &= NBP + disturbance + R_h + R_a \end{aligned} \quad (1)$$

where *GPP* is the gross primary production, *NPP* the net primary production, R_a the autotrophic respiration, *NEP* the net ecosystem production, R_h the heterotrophic respiration, *NBP* the net biome production, and *disturbance* includes anthropogenic emissions due to land cover and land use changes such as fires and crop harvest. In this study, *GPP, NPP, NEP, NBP,* R_a, and R_h are direct outputs from GLENS while *disturbance* is estimated by subtracting *NBP* from *NEP*. Positive values for *GPP, NPP, NEP*, and *NBP* indicate carbon gains in land while negative values denote carbon losses to the atmosphere; contrarily, positive values for R_a and R_h represent carbon losses to the atmosphere and larger negative values imply more carbon remaining in land. We utilize *NBP* to examine the carbon storage in terrestrial ecosystems. A positive *NBP* value indicates atmospheric CO_2 is stored in the terrestrial ecosystem while a negative *NBP* value represents carbon releases from the terrestrial ecosystem to the atmosphere. A fixed ratio of 1:2.13 (Clark 1982, O'Hara 1990) is used in this study to convert the amount of carbon (unit: Pg C) released from or sequestered in the terrestrial ecosystem to the

equivalent amount of airborne CO_2 mole fractions (unit: ppm).

Simulations in GLENS were driven by the atmospheric CO_2 mole fraction specified in the RCP8.5 emission scenario (Meinshausen *et al* 2011, Riahi *et al* 2011). The simulations were conducted with an active global land carbon cycle; however, the terrestrial BGC feedbacks were not incorporated into the coupled modeling system. In addition, the marine BGC feedbacks were excluded in the GLENS experiments. We assume the *NBP* variations are consistent with the atmospheric CO_2 for the *CTRL* experiment. Hence, differences in simulated *NBP* between *GEOENG* and *CTRL* are attributed to ecosystem responses due to SO_2 injections in the lower stratosphere. A positive value of these differences, *i.e.* a larger accumulated *NBP* in *GEOENG* than in *CTRL* indicates more carbon is stored from the atmosphere to land, thus the atmospheric CO_2 level is lowered; on the contrary, the atmospheric CO_2 level is higher when less carbon is sequestered in land due to lower accumulated *NBP* in *GEOENG* than in *CTRL*. To construct an adjusted atmospheric CO_2 trajectory that accounts for this feedback, we compute the adjusted CO_2 airborne mole fraction every year according to the equation

$$C_{t+1} = C_t + (F_{t+1} - F_t) + (B_{t,GEOENG} - B_{t,CTRL}) \quad (2)$$

where t is the time step, C the adjusted atmospheric CO_2 airborne mole fractions, F the atmospheric CO_2 airborne mole fractions obtained from GLENS outputs, and B the terrestrial BGC feedbacks from experiment *GEOENG* and *CTRL*. The changes in the atmospheric CO_2 trajectory alter the radiative forcing, resulting in a different surface temperature trajectory. The changes in surface temperatures due to atmospheric CO_2 adjustments are approximated through an impulse response function tuned to the mean of CMIP5 models (Boucher and Reddy 2008, Hoffman *et al* 2014). We use this function to compute CO_2-induced radiative forcing changes and thus the associated temperature trajectory adjustments. Differences between the simulated global mean surface temperature in GLENS and the adjusted one are compared to estimate a reduced amount of SO_2 injection, with an injection rate of 10 Tg SO_2 per year for 1 K cooling (Tilmes *et al* 2018).

3. Results and discussion

3.1. Global climate changes

Global mean surface temperatures are projected higher in *CTRL* than in *BASE* due to rising greenhouse gas levels as previously reported (IPCC 2014) (figure 2(a)). In *GEOENG*, slightly higher mean surface temperatures in the Sahara Desert and at mid-to-high latitudes compared to *BASE* (figure 2(b)) are compensated by lower surface temperatures in the central US, parts of South America, Central Asia, southern India, and eastern Australia. The global mean surface temperatures in *GEOENG* are lower compared to *CTRL* despite having the same greenhouse gas trajectories as a result of stratospheric aerosol injections (figure 2(c)). Higher precipitation rates are projected in most regions in *CTRL* than in *BASE* due to increased water vapor content in the lower troposphere and atmospheric circulation, both of which are induced by the increased temperature in the *CTRL* simulation (Collins *et al* 2013); lower precipitation rates are simulated in the Amazon Basin, Chile and Argentina, Uruguay, western Congo, southern Africa, some southern parts of Europe, and Indonesia (figure 2(d)). The results are consistent with known features of projected climate change (IPCC 2014, Yu *et al* 2016). The regions with lower precipitation rates in *CTRL* than in *BASE*, which include forests, croplands, and open shrublands (see figure 1), are influenced by changing atmospheric dynamics (Yoon and Zeng 2010) and physiological responses (Langenbrunner *et al* 2019) along with enhanced direct solar radiation but reduced diffuse solar radiation (figures 2(g) and (j)). In *GEOENG*, cooler temperatures, reduced evapotranspiration, and aerosol-cloud interactions (suppressed precipitation due to the aerosol indirect effect (Albrecht 1989)) lead to a drier climate compared to *BASE* over the southern Sahel and South Africa, India, Southeast Asia, and parts of the boreal zone across Eurasia and northeastern North America (figure 2(e)). Global mean precipitation rates in *GEOENG* are generally smaller than that in *CTRL* (figure 2(f)) due to lower temperatures and induced suppression of precipitation, with the exception of the southern Amazon (evergreen broadleaf forests) (Langenbrunner *et al* 2019) and semi-arid and monsoon regions (Tilmes *et al* 2013), including the western U.S. (open shrublands), southern Africa (open shrublands), eastern Australia (open shrublands), southern Europe/northern Africa/western Asia (open shrublands/sparsely vegetated lands).

In terms of downward solar radiation at the surface, direct radiation is 109.4 ± 0.3 W m^{-2} for *BASE* in 2019, 111.5 ± 1.0 W m^{-2} for *CTRL* and 79.8 ± 1.2 W m^{-2} for *GEOENG* in 2097; diffuse radiation is 61.6 ± 0.1 W m^{-2} for *BASE* in 2019, 58.3 ± 0.4 W m^{-2} for *CTRL* and 83.0 ± 0.8 W m^{-2} for *GEOENG* in 2097. More direct radiation is projected in *CTRL* compared to *BASE* in most regions except for India, northern and central Africa, central South America, and the southeast US (figure 2(g)). Reductions in cloudiness (figure S1) are the primary explanation for such direct radiation changes (spatial correlation $= -0.76$), which is consistent with the results from Yu *et al* (2016). Nevertheless, regions like northeast Australia experience increased downward direct radiation despite increasing cloudiness due to enhanced precipitation (figure 2(d)) that removes suspended aerosols from the atmosphere (*i.e.* reduced

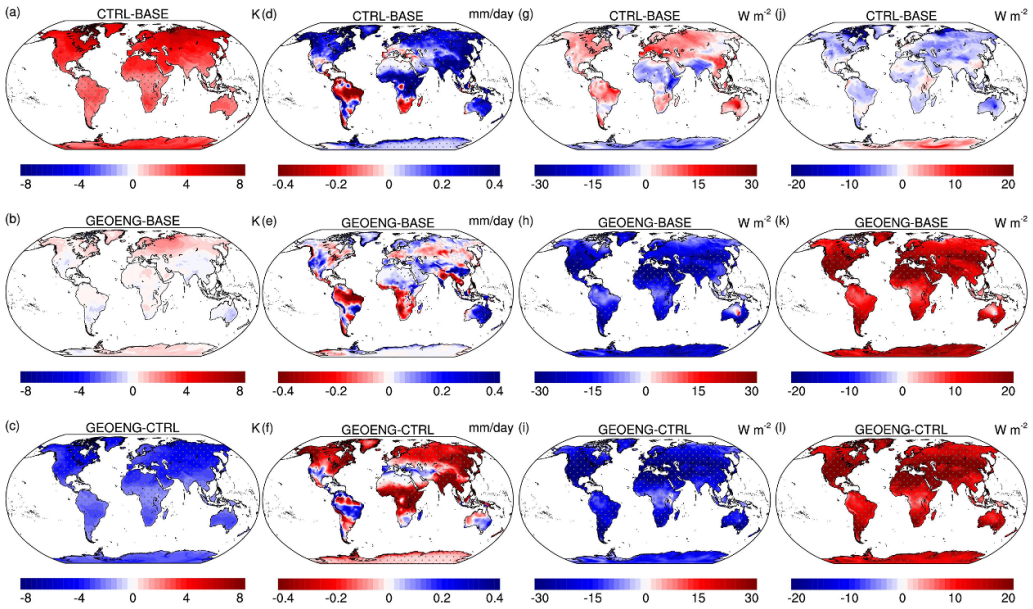

Figure 2. Changes of spatial distributions between *CTRL* and *BASE* (top row), between *GEOENG* and *BASE* (middle row), and between *GEOENG* and *CTRL* (bottom row) for surface temperature (K, (a)–(c)), precipitation (mm day^{-1}, (d)–(f)), total downward direct solar radiation at the surface (W m^{-2}, (g)–(i)), and total downward diffuse solar radiation at the surface (W m^{-2}, (j)–(l)). The spatial distribution of *CTRL* is from the 2020–2097 time-averaged results without geoengineering while that of *GEOENG* is from the 2020–2097 time-averaged results with geoengineering applied. The spatial distribution of *BASE* is from the 2010–2019 time-average results. Light grey stippling (dots) indicates regions where the change is significant using the Student's *t*-test ($p < 0.1$).

aerosol optical depth (AOD), figure S2). Reduced diffuse radiation at the surface (figure 2(j)) is associated with the reduction of total cloudiness in most regions. On the other hand, *GEOENG* shows decreased direct radiation and increased diffuse radiation at the surface with respect to *BASE* (figures 2(h) and (k)) because of increased amounts of aerosols suspended in the atmosphere due to SO_2 injections. An unexpected increase in surface radiation in the dust region of central Australia in *GEOENG* compared to *BASE* (figure 2(h)), similar to that described above when comparing *CTRL* with *BASE*, is caused by lower dust emission (figures S3 and S4) because of wetter climate conditions (figure 2(e)). In this region, the spatial correlation is −0.94 between precipitation and coarse mode dust AOD, and that between precipitation and Aitken mode dust AOD is −0.59. Differences in downward solar radiation at the surface between *GEOENG* and *CTRL* are associated with higher aerosol amounts due to SO_2 injections, which block direct radiation and enhance diffuse radiation (figures 2(i) and (l)).

3.2. Global terrestrial biogeochemical responses

Photosynthesis rates (*FPSN*) and *GPP* for both *CTRL* and *GEOENG* substantially increase in most of the world because of rising atmospheric CO_2 levels with respect to *BASE* (figures 3(a), (b), (d), and (e)). At high latitudes, *FPSN* and *GPP* are lower in *BASE* and in *GEOENG* than in *CTRL* because higher surface temperatures in *CTRL* (figure 2(c)) thaw permafrost regions, lengthen growing seasons and enable enhanced photosynthesis (figures 3(a) and (c)). At mid and low latitudes, lower precipitation and less diffuse radiation in the Amazon Basin and southern Africa produce lower *FPSN* and *GPP* in *CTRL* than in *BASE* (figures 3(a) and (d)). In addition, lower *FPSN* and *GPP* in India and central Africa, where land cover is dominated by croplands and savannas, are subjected to lower precipitation in *BASE* and in *GEOENG* than in *CTRL* (figures 2(d) and (f)). However, substantial *FPSN* and *GPP* increases in *GEOENG* with respect to *CTRL* are found in the southwestern U.S. (open shrublands), southern Amazon (woody savannas), France/Spain/northern Africa (croplands and open shrublands), southern Africa (open shrublands), central Russia (mixed forests), and eastern Australia (open shrublands) (figure 3(f)). Such increases in *FPSN* and *GPP* are associated with increased precipitation and soil moisture (see figure 2(f) and supplementary figure S5). While the projected spatial *GPP* patterns are consistent with previous studies (Kalidindi *et al* 2015, Tjiputra *et al* 2016, Dagon and Schrag 2019), different spatial patterns are found between *FPSN* and *GPP* across the Amazon Basin for changes between *GEOENG* and *CTRL* (figures 3(c) and (f)). Since the terrestrial nitrogen cycle has been suggested to be a critical factor for the carbon cycle response (Tjiputra *et al* 2016), we investigate the spatial pattern of net nitrogen mineralization (supplementary figure S6) and find that the inconsistent spatial patterns between *FPSN* and *GPP* are where net nitrogen mineralization is smaller in *GEOENG* than in *CTRL*. This is mainly because

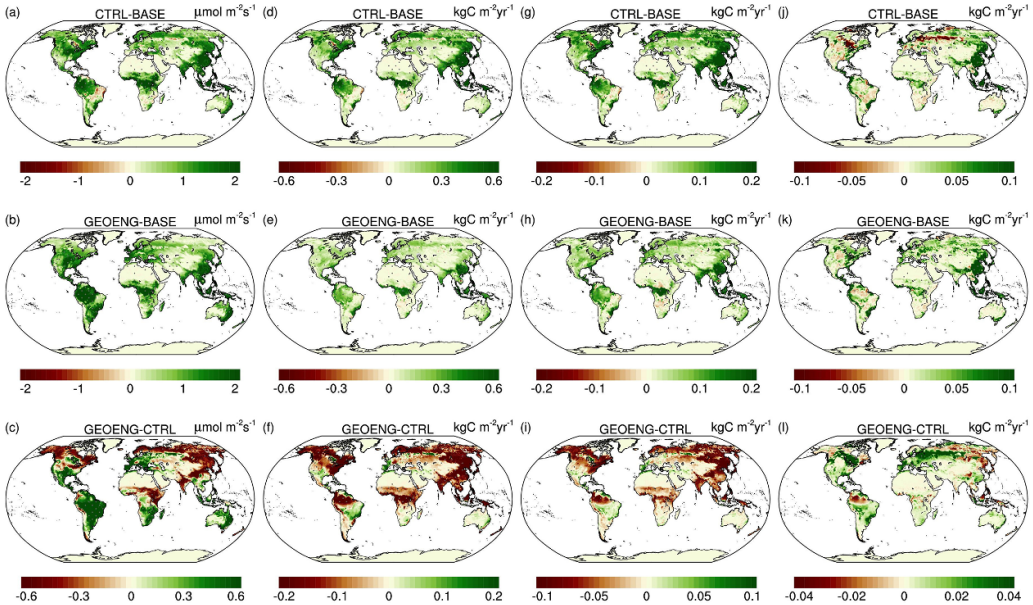

Figure 3. Changes of spatial distributions between *CTRL* and *BASE* (top row), between *GEOENG* and *BASE* (middle row), and between *GEOENG* and *CTRL* (bottom row) for photosynthesis rates (μmol m^{-2} s^{-1}, (a)–(c)), gross primary production (kg C m^{-2} yr^{-1}, (d)–(f)), net primary production (kg C m^{-2} yr^{-1}, (g)–(i)), and net biome production (kg C m^{-2} yr^{-1}, (j)–(l)). The spatial distribution of *CTRL* is from the 2020–2097 time-averaged results without geoengineering while that of *GEOENG* is from the 2020–2097 time-averaged results with geoengineering applied. The spatial distribution of *BASE* is from the 2010–2019 time-average results. Light grey stippling (dots) indicates regions where the change is significant using the Student's *t*-test ($p < 0.1$).

lower temperatures in *GEOENG* produce lower net nitrogen mineralization rates, reducing conversion of organic nitrogen to a plant-available inorganic form and hence downregulating photosynthesis.

Enhanced R_a in *CTRL* and in *GEOENG* with respect to *BASE* are caused by enhanced *GPP*, which is attributed to the CO_2 fertilization effect (see supplementary figure S7). Lower R_a in *GEOENG* than in *CTRL* is primarily caused by the cooler climate in *GEOENG*. *NPP*, which is determined by *GPP* and R_a (see equation (1)), increases in both *CTRL* and *GEOENG* compared to *BASE* (figures 3(g) and (h)). Stronger reductions in *GPP* than in R_a result in lower *NPP* in *GEOENG* with respect to *CTRL* (figure 3(i)). Like R_a is sensitive to temperatures and *GPP* variations, R_h is sensitive to changes in temperature and the carbon amounts in litter and soil. Higher rates of *GPP* in *CTRL* and *GEOENG* compared to *BASE* drive higher rates of R_h because of larger litter inputs that also increased soil pools (see supplementary figure S8). Therefore, higher R_h is simulated in both *CTRL* and *GEOENG* compared to *BASE* in most regions (see supplementary figure S9). Nevertheless, regions with reduced precipitation and lower temperatures in *GEOENG* than in *CTRL*, such as the northern Amazon, undergo lower R_h and evapotranspiration rates in *GEOENG*, which in turn retains more water in soil due to stomatal closure in plants (Swann *et al* 2016) (see supplementary figures S5 and S10).

The spatial patterns of *NEP* are determined by *NPP* and R_h. Both *CTRL* and *GEOENG* demonstrate enhanced *NEP* compared to *BASE* with the exception of North America. Higher *NPP* induces higher *NEP* in *CTRL* and in *GEOENG* with respect to *BASE*; however, stronger increases of R_h due to land use change and accelerated litter input than the increases of *NPP* in North America cause reduced *NEP* in both *CTRL* and *GEOENG* when compared to *BASE* (see supplementary figure S11). Similar to *NPP*, the cooler climate in *GEOENG* leads to lower *NEP* than that of *CTRL*. The variations of *NEP* and *disturbance* determine the perturbations of *NBP*, which represents the long-term and large-scale carbon uptake by ecosystems (see equation (1)). In GLENS outputs, *disturbance* is excluded in *NEP* but is included in *NBP*. Hence, differences in the spatial patterns between *NBP* and *NEP* illustrate the human and natural disturbances. In general, *CTRL* and *GEOENG* simulate enhanced *NBP* attributed to stronger *GPP* than in *BASE* (figures 3(j) and (k)); smaller *NBP* over North America in *CTRL* than in *BASE* is caused by increased carbon loss due to fires (see supplementary figures S12 and S13). Similarly, smaller burned area and lower carbon loss due to fires in *GEOENG* explain the enhanced *NBP* in North America, the boreal region of Eurasia, and the southeast coast of Australia with respect to *CTRL* (figure 3(l)).

3.3. Carbon sink strength and atmospheric CO_2 trajectory adjustments

The carbon sink strength (CSS) is determined by the accumulated *NBP* over a certain period of time. Table 1 lists the accumulated global carbon amount changes over various time periods for each carbon fluxes in

Table 1. Accumulated global climate change over various time periods. Numbers represent the mean and cross-ensemble standard deviation of the first three ensemble members for the *BASE*, *CTRL*, and *GEOENG* (abbreviated as *GEOG*). *PRECIP* and *ET* are precipitation and evapotranspiration (unit: mm day^{-1}), respectively, and the other variable annotations (unit: Pg C) are the same as equation (1). Positive values for *GPP*, *NPP*, *NEP*, and *NBP* indicate carbon gains in ecosystems while negative values represent carbon losses to the atmosphere; the opposite applies to R_a and R_h. Symbol ' ' denotes the differences of *GEOENG* − *CTRL*. The asterisk sign (*) indicates 2011–2019 cumulative sum.

Variable	2010–2019	2020–2097			2020–2039			2050–2069			2078–2097		
	BASE	*CTRL*	*GEOG*	Δ	*CTRL*	*GEOG*	Δ	*CTRL*	*GEOG*	Δ	*CTRL*	*GEOG*	Δ
GPP	1153 ± 7	11 085 ± 27	10 271 ± 7	−813 ± 21	2497 ± 15	2474 ± 5	−23 ± 11	2863 ± 5	2648 ± 8	−215 ± 7	3176 ± 9	2783 ± 2	−393 ± 9
NPP	499 ± 3	4700 ± 8	4442 ± 3	−258 ± 5	1072 ± 4	1067 ± 2	−5 ± 2	1216 ± 2	1146 ± 4	−69 ± 4	1329 ± 3	1205 ± 2	−124 ± 3
NEP	51 ± 2	602 ± 2	585 ± 2	−17 ± 3	128 ± 1	136 ± 1	7 ± 1	159 ± 1	154 ± 1	−4 ± 1	173 ± 3	160 ± 1	−14 ± 2
NBP	4 ± 2*	198 ± 4	277 ± 3	79 ± 6	50 ± 1	62 ± 1	13 ± 2	56 ± 1	77 ± 1	20 ± 2	43 ± 4	73 ± 0	30 ± 3
R_a	654 ± 4	6385 ± 20	5830 ± 4	−555 ± 16	1425 ± 11	1407 ± 3	−18 ± 8	1648 ± 3	1502 ± 5	−146 ± 4	1847 ± 6	1579 ± 0	−269 ± 6
R_h	448 ± 2	4098 ± 6	3856 ± 2	−241 ± 4	944 ± 4	931 ± 1	−13 ± 3	1057 ± 2	992 ± 3	−65 ± 4	1155 ± 1	1045 ± 1	−110 ± 2
Disturbance	42 ± 1*	405 ± 2	308 ± 1	−96 ± 3	79 ± 1	74 ± 1	−5 ± 1	103 ± 1	78 ± 0	−25 ± 2	130 ± 1	86 ± 0	−44 ± 1
PRECIP	24 ± 0	199 ± 0	184 ± 0	−15 ± 1	48 ± 0	47 ± 0	−1 ± 0	51 ± 0	47 ± 0	−4 ± 1	53 ± 0	47 ± 0	−7 ± 0
ET	14 ± 0	120 ± 0	110 ± 0	−10 ± 0	29 ± 0	29 ± 0	−1 ± 0	31 ± 0	28 ± 0	−3 ± 0	32 ± 0	28 ± 0	−5 ± 0

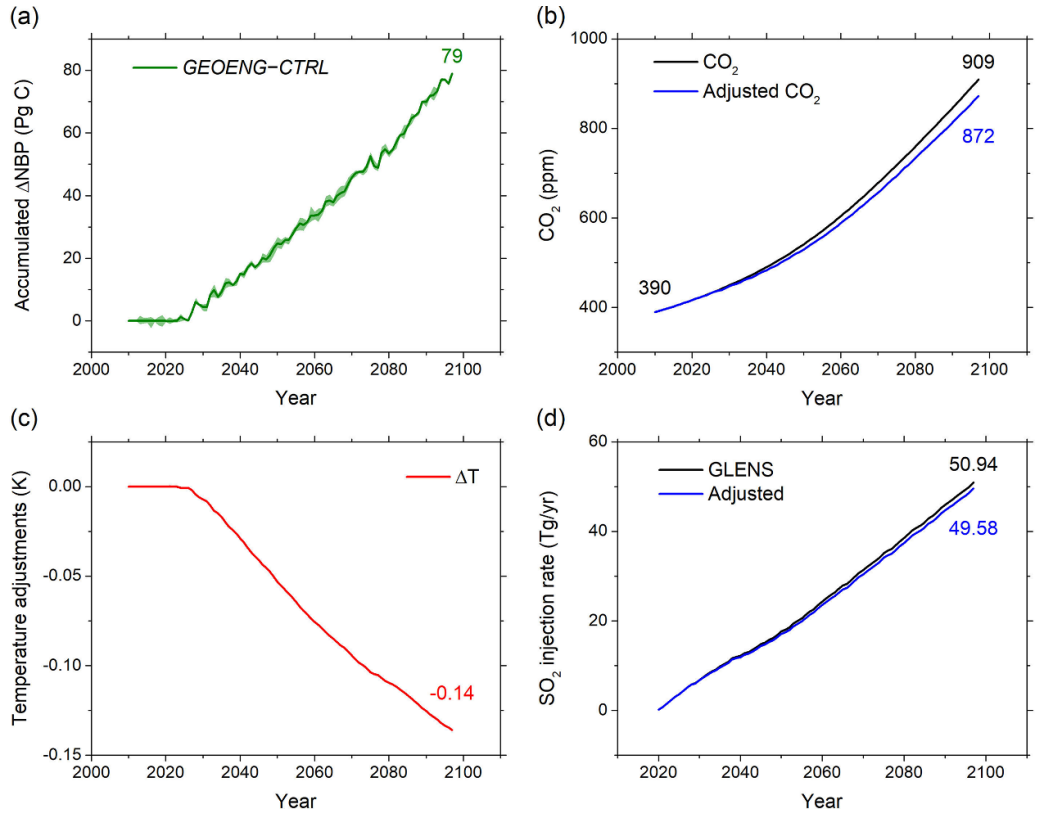

Figure 4. The trajectories of (a) accumulated global carbon sink strength changes (Pg C) due to geoengineering, (b) the atmospheric CO_2 mole fraction (ppm) during 2010–2097 for *BASE* + *CTRL* (black line) and the adjusted atmospheric CO_2 mole fraction due to terrestrial BGC feedbacks under geoengineering (blue line), (c) surface temperature responses (K) due to atmospheric CO_2 adjustments, and (d) sulfur injection rates (Tg yr^{-1}) in GLENS (red) and adjusted injection rates due to terrestrial BGC feedbacks (blue).

equation (1). The terrestrial ecosystem has higher global total *GPP* primarily due to elevated CO_2 levels in both *CTRL* and *GEOENG* with respect to *BASE*. All the other terrestrial carbon fluxes except *NBP* in the terrestrial carbon budget (see equation (1)) are enhanced over time in both *CTRL* and *GEOENG*. Increases of *GPP, NPP, NEP,* R_a, and R_h in *GEOENG* are slower compared to *CTRL* because of lower temperatures and lower precipitation rates in *GEOENG*. Differences of accumulated *NBP* between *GEOENG* and *CTRL* show stronger CSS in *GEOENG* than in *CTRL* by 79 ± 6 Pg C at year 2097, increasing from 13 ± 2 Pg C during 2020–2039 to 30 ± 3 Pg C during 2078–2097. Such CSS enhancement is attributed primarily to reduced R_a and R_h, which leaves more carbon resident in land globally. Additionally, smaller carbon losses due to natural or anthropogenic disturbances (estimated by *NEP*−*NBP*) in *GEOENG* also indicate a larger land carbon reservoir.

For individual ecoregions, about 63% (125 ± 1 Pg C) of global *NBP* (198 ± 4 Pg C) in *CTRL* and 47% (130 ± 1 Pg C) of global *NBP* (277 ± 3 Pg C) in *GEOENG* during 2020–2097 are contained in evergreen broadleaf forests in tropical regions, which have the largest CSS among all ecoregions (see supplementary table S1). Nevertheless, the largest CSS differences (ΔCSS) between *GEOENG* and *BASE* are found in croplands and mixed forests (see supplementary figure S14). The former are responsible for 27% (22 ± 2vPg C) and the latter for 25% (19 ± 0 Pg C) of the total ΔCSS (79 ± 6 Pg C) by 2097. Less heat stress due to lower temperatures in *GEOENG* than in *CTRL* is the main factor that increases crop yields (*i.e.* more carbon gains on land) in spite of lower precipitation (Proctor *et al* 2018). Increases in ΔCSS are also simulated in all other vegetated ecoregions during 2020–2097, primarily as a result of reduced respiration rates. Most ecoregions in both *CTRL* and *GEOENG* undergo increasing CSS from 2020–2039 to 2050–2069 but declined CSS from 2050–2069 to 2078–2097. Land use changes due to forest clearing and conversions to agriculture in the RCP8.5 emission scenario are likely the cause of these CSS changes (Hurtt *et al* 2011).

The changes in ΔCSS provide information to reconstruct the atmospheric CO_2 trajectory in GLENS experiments in which the same atmospheric CO_2 mole fractions based on the RCP8.5 emission scenario were used to drive the simulations. Even though carbon pools were simulated with an active terrestrial carbon cycle, terrestrial BGC feedbacks to the Earth system were not accounted for in the coupled modeling system. Such feedbacks can alter the carbon amount in the atmosphere, resulting in a

different atmospheric CO_2 trajectory and hence climate change. Given the assumption that the land carbon fluxes in *CTRL* are consistent with the specified atmospheric CO_2 trajectory, we evaluate carbon gains on land as a result of aerosol geoengineering through comparing ΔCSS between *GEOENG* and *CTRL* (figure 4(a)). The global ΔCSS reaches 79 ± 6 Pg C by 2097. That is, terrestrial ecosystems globally store additional carbon in *GEOENG* compared to *CTRL*, amounting to 37 ± 3 ppm CO_2-equivalent, reducing the atmospheric CO_2 mole fraction by as much as 4% in 2097 (figure 4(b)). The reduced airborne fraction of anthropogenic carbon due to terrestrial BGC feedbacks is within the range reported in previous studies by the year 2100 despite different models and aerosol geoengineering strategies compared with GLENS (Keller *et al* 2014, Tjiputra *et al* 2016, Cao and Jiang 2017).

By accounting for the terrestrial BGC feedback, lower atmospheric CO_2 levels would induce a cooler global surface temperature in *GEOENG* compared to the prescribed CO_2 trajectory, differing by 0.14 K in 2097 (figure 4(c)). Hence, in order to maintain the global surface temperature at 2020-levels, less sulfur aerosol would have needed to be injected (approximately 1.4 Tg yr^{-1} less at 2097) had we used prescribed emissions rather than prescribed concentrations in GLENS (figure 4(d)). In addition, the global carbon budget assessment indicates that annual anthropogenic carbon emissions are stored 31% in land, 23% in the ocean, and 46% in the atmosphere (Friedlingstein *et al* 2019). Thus, the atmospheric CO_2 trajectory, altered slowly by additional carbon uptake on land, would effectively reduce ocean carbon uptake, thereby partially compensating for the reductions in atmospheric CO_2 mole fraction. In general, marine CSS is enhanced in a cooler climate that maintains higher CO_2 solubility and stronger overturning circulation in oceans; however, increasing anthropogenic ocean acidification would likely mediate marine CSS due to its detrimental effects on calcifying biota (Orr *et al* 2005, Fabry *et al* 2008, Doney *et al* 2009, Gattuso *et al* 2015). While fully coupled emissions-forced simulations with interactive terrestrial and marine biogeochemistry are required to quantify competing feedback effects, we expect that temperature-induced reduction of the solubility pump in *CTRL* simulations would be responsible for stronger marine CSS in *GEOENG* simulations; however, over decadal timescales (out to 2100), we expect a smaller ocean feedback compared to the land feedback in *GEOENG*, consistent with other studies (Keller *et al* 2014, Cao and Jiang 2017).

4. Conclusion

This study characterizes responses and feedbacks of terrestrial ecosystems from an ensemble of coupled high-resolution Earth system model climate change simulations under a high greenhouse gas scenario with a geoengineering mitigation strategy that completely offsets temperature warming due to elevated anthropogenic CO_2. From the GLENS simulation results, we find that terrestrial ecosystems could store an additional 79 Pg C on land globally by the end of the twenty-first century due to SO_2 injections in the lower stratosphere. Such carbon gains on land are mainly attributed to lower ecosystem respiration and diminished disturbance effects under geoengineering. As a result, less geoengineering effort would be needed to maintain the global surface temperature at 2020-levels in GLENS. Since GLENS simulated with an active terrestrial carbon cycle but without marine BGC feedbacks, we suggest that conducting fully coupled and emissions-forced ESM simulations with both marine and terrestrial BGC feedbacks enabled, as well as including stratospheric and tropospheric chemistry, will be necessary to reduce the uncertainty in quantifying aerosol geoengineering impacts on the Earth system.

Acknowledgments

This research was supported by the Reducing Uncertainties in Biogeochemical Interactions through Synthesis and Computation (RUBISCO) Science Focus Area (SFA), which is sponsored by the Regional and Global Model Analysis activity of the Earth & Environmental Systems Modeling Program in the Earth and Environmental Systems Sciences Division (EESSD) of the Office of Biological and Environmental Research (BER) in the US Department of Energy Office of Science. This research was also supported by the Oak Ridge National Laboratory Terrestrial Ecosystem Sciences (TES) SFA, sponsored by the Terrestrial Ecosystem Sciences program, which is also part of EESSD in BER in the US Department of Energy Office of Science. This research used resources of the Oak Ridge Leadership Computing Facility (OLCF) at Oak Ridge National Laboratory (ORNL), which is managed by UT-Battelle, LLC, for the US Department of Energy under Contract No. DE-AC05-00OR22725. Support for B.K. was provided in part by the National Science Foundation through agreement CBET-1931641, the Indiana University Environmental Resilience Institute, and the *Prepared for Environmental Change* Grand Challenge initiative. The Pacific Northwest National Laboratory is operated for the US Department of Energy by Battelle Memorial Institute under contract DE-AC05-76RL01830. Support for L.X. was provided by the National Science Foundation grant AGS-1617844. The CESM project is supported primarily by the National Science Foundation (NSF). This material is based work supported by the National Center for Atmospheric Research, which is a major facility sponsored by the NSF under Cooperative

Agreement No. 1852977. Computing and data storage resources, including the Cheyenne supercomputer (doi:10.5065/D6RX99HX), provided by the Computational and Information Systems Laboratory (CISL) at NCAR. All simulations were carried out on the Cheyenne high-performance computing platform https://www2.cisl.ucar.edu/user-support/acknowledging-ncarcisl and are available to the community via the Earth System Grid.

Contributions

C-EY performed the analysis, generated graphical results, and prepared the manuscript in consultation with FH, JF, LX, and DR. FH provided impulse response function calculations. ST, DM, JR, MM, BK were the core team conducting the model simulations in GLENS. All authors contributed to group discussions and manuscript revisions.

Conflict of interests

The authors declare no competing interests.

Data availability statement

The data that support the findings of this study are openly available at the following URL/DOI: https://doi.org/10.5065/D6JH3JXX.

Code availability

All figures were generated using the NCAR Command Language version 6.6.2 (available at https://doi.org/10.5065/D6WD3XH5) and OriginPro version 2019b (available at www.originlab.com). Scripts used in this study are available on request from cyang10@vols.utk.edu.

ORCID iDs

Cheng-En Yang https://orcid.org/0000-0002-4069-4997
Forrest M Hoffman https://orcid.org/0000-0001-5802-4134
Daniel M Ricciuto https://orcid.org/0000-0002-3668-3021
Simone Tilmes https://orcid.org/0000-0002-6557-3569
Lili Xia https://orcid.org/0000-0001-7821-9756
Douglas G MacMartin https://orcid.org/0000-0003-1987-9417
Ben Kravitz https://orcid.org/0000-0001-6318-1150
Jadwiga H Richter https://orcid.org/0000-0001-7048-0781
Michael Mills https://orcid.org/0000-0002-8054-1346
Joshua S Fu https://orcid.org/0000-0001-5464-9225

References

Albrecht B A 1989 Aerosols, cloud microphysics, and fractional cloudiness *Science* **245** 1227–30
Bala G, Duffy P B and Taylor K E 2008 Impact of geoengineering schemes on the global hydrological cycle *Proc. Natl Acad. Sci. USA* **105** 7664–9
Boucher O and Reddy M S 2008 Climate trade-off between black carbon and carbon dioxide emissions *Energy Policy* **36** 193–200
Cao L and Jiang J 2017 Simulated effect of carbon cycle feedback on climate response to solar geoengineering *Geophys. Res. Lett.* **44** 12,484–12,491
Cheng W, Macmartin D G, Dagon K, Kravitz B, Tilmes S, Richter J H, Mills M J and Simpson I R 2019 Soil moisture and other hydrological changes in a stratospheric aerosol geoengineering large ensemble *J. Geophys. Res. Atmos.* **124** 12773–93
Clark W C 1982 *Carbon Dioxide Review* (Oxford: Oxford University Press) (https://www.osti.gov/biblio/5963903-carbon-dioxide-review)
Collins M *et al* 2013 Long-term climate change: projections, commitments and irreversibility *Climate Change 2013: The Physical Science Basis. Contribution of Working Group I to the Fifth Assessment Report of the Intergovernmental Panel on Climate Change*, ed T F Stocker *et al* (Cambridge: Cambridge University Press) pp 1029–136 (https://www.ipcc.ch/report/ar5/wg1)
Crutzen P J 2006 Albedo enhancement by stratospheric sulfur injections: a contribution to resolve a policy dilemma? *Clim. Change* **77** 211–20
Dagon K and Schrag D P 2019 Quantifying the effects of solar geoengineering on vegetation *Clim. Change* **153** 235–51
Danabasoglu G, Bates S C, Briegleb B P, Jayne S R, Jochum M, Large W G, Peacock S and Yeager S G 2012 The CCSM4 ocean component *J. Clim.* **25** 1361–89
Doney S C, Fabry V J, Feely R A and Kleypas J A 2009 Ocean acidification: the other CO_2 problem *Annu. Rev. Mar. Sci.* **1** 169–92
Duan L, Cao L, Bala G and Caldeira K 2020 A model-based investigation of terrestrial plant carbon uptake response to four radiation modification approaches *J. Geophys. Res. Atmos.* **125** e2019JD031883
Fabry V J, Seibel B A, Feely R A and Orr J C 2008 Impacts of ocean acidification on marine fauna and ecosystem processes *ICES J. Mar. Sci.* **65** 414–32
Fasullo J T, Tilmes S, Richter J H, Kravitz B, Macmartin D G, Mills M J and Simpson I R 2018 Persistent polar ocean warming in a strategically geoengineered climate *Nat. Geosci.* **11** 910–4
Friedlingstein P *et al* 2019 Global carbon budget 2019 *Earth Syst. Sci. Data* **11** 1783–838
Gattuso J-P *et al* 2015 Contrasting futures for ocean and society from different anthropogenic CO_2 emissions scenarios *Science* **349** aac4722
Gu L, Baldocchi D D, Wofsy S C, Munger J W, Michalsky J J, Urbanski S P and Boden T A 2003 Response of a deciduous forest to the Mount Pinatubo eruption: enhanced photosynthesis *Science* **299** 2035–8
Hargrove W W, Hoffman F M and Hessburg P F 2006 Mapcurves: a quantitative method for comparing categorical maps *J. Geogr. Syst.* **8** 187–208
Hargrove W W and Hoffman F M 2004 Potential of multivariate quantitative methods for delineation and visualization of ecoregions *Environ. Manage.* **34** S39–60
Hoegh-Guldberg O *et al* 2018 Impacts of 1.5°C global warming on natural and human systems *Global Warming of 1.5°C. An IPCC Special Report on the Impacts of Global Warming of*

1.5° C above Pre-industrial Levels and Related Global Greenhouse Gas Emission Pathways, in the Context of Strengthening the Global Response to the Threat of Climate Change, Sustainable Development, and Efforts to Eradicate Poverty, ed V Masson-Delmotte *et al* (Intergovernmental Panel on Climate Change) (https://www.ipcc.ch/sr15/download/)

Hoffman F M *et al* 2014 Causes and implications of persistent atmospheric carbon dioxide biases in Earth system models *J. Geophys. Res. Biogeosci.* **119** 141–62

Hunke E C and Lipscomb W H 2008 CICE: The Los Alamos sea ice model documentation and software user's manual version 4.0 (http://www.cesm.ucar.edu/models/cesm1.0/cice/ice_usrdoc.pdf)

Hurtt G C *et al* 2011 Harmonization of land-use scenarios for the period 1500–2100: 600 years of global gridded annual land-use transitions, wood harvest, and resulting secondary lands *Clim. Change* **109** 117–61

IPCC 2001 *Climate Change 2001: The Scientific Basis* Cambridge University Press, New York

IPCC 2014 *Climate Change 2014: Synthesis Report* IPCC, Geneva, Switzerland (https://www.ipcc.ch/report/ar5/sy)

Kalidindi S, Bala G, Modak A and Caldeira K 2015 Modeling of solar radiation management: a comparison of simulations using reduced solar constant and stratospheric sulphate aerosols *Clim. Dyn.* **44** 2909–25

Keith D W, Wagner G and Zabel C L 2017 Solar geoengineering reduces atmospheric carbon burden *Nat. Clim. Change* **7** 617–9

Keller D P, Feng E Y and Oschlies A 2014 Potential climate engineering effectiveness and side effects during a high carbon dioxide-emission scenario *Nat. Commun.* **5** 3304

Kravitz B *et al* 2013 Climate model response from the geoengineering model intercomparison project (GeoMIP) *J. Geophys. Res. Atmos.* **118** 8320–32

Kravitz B, Macmartin D G, Mills M J, Richter J H, Tilmes S, Lamarque J, Tribbia J J and Vitt F 2017 First simulations of designing stratospheric sulfate aerosol geoengineering to meet multiple simultaneous climate objectives *J. Geophys. Res. Atmos.* **122** 12,616–12,634

Kravitz B, Macmartin D G, Wang H and Rasch P J 2016 Geoengineering as a design problem *Earth Syst. Dyn.* **7** 469–97

Kravitz B, Robock A, Oman L, Stenchikov G and Marquardt A B 2009 Sulfuric acid deposition from stratospheric geoengineering with sulfate aerosols *J. Geophys. Res.* **114** D14109

Langenbrunner B, Pritchard M S, Kooperman G J and Randerson J T 2019 Why does amazon precipitation decrease when tropical forests respond to increasing CO_2? *Earths Future* **7** 450–68

Macmartin D G, Kravitz B, Keith D W and Jarvis A 2014 Dynamics of the coupled human–climate system resulting from closed-loop control of solar geoengineering *Clim. Dyn.* **43** 243–58

Meinshausen M *et al* 2011 The RCP greenhouse gas concentrations and their extensions from 1765 to 2300 *Clim. Change* **109** 213–41

Mercado L M, Bellouin N, Sitch S, Boucher O, Huntingford C, Wild M and Cox P M 2009 Impact of changes in diffuse radiation on the global land carbon sink *Nature* **458** 1014–7

Mills M J *et al* 2017 Radiative and chemical response to interactive stratospheric sulfate aerosols in fully coupled CESM1(WACCM) *J. Geophys. Res. Atmos.* **122** 13,061–13,078

Moore J C *et al* 2014 Arctic sea ice and atmospheric circulation under the GeoMIP G1 scenario *J. Geophys. Res. Atmos.* **119** 567–83

Moreno-Cruz J B and Keith D W 2013 Climate policy under uncertainty: a case for solar geoengineering *Clim. Change* **121** 431–44

Oleson K W *et al* 2013 *Technical Description of Version 4.5 Of the Community Land Model (CLM)* (Boulder, CO, USA: National Center for Atmospheric Research) (https://doi.org/10.5065/D6RR1W7M)

Orr J C *et al* 2005 Anthropogenic ocean acidification over the twenty-first century and its impact on calcifying organisms *Nature* **437** 681–6

O'Hara F N 1990 Glossary: Carbon Dioxide and Climate

Proctor J, Hsiang S, Burney J, Burke M and Schlenker W 2018 Estimating global agricultural effects of geoengineering using volcanic eruptions *Nature* **560** 480–3

Riahi K, Rao S, Krey V, Cho C, Chirkov V, Fischer G, Kindermann G, Nakicenovic N and Rafaj P 2011 RCP 8.5—a scenario of comparatively high greenhouse gas emissions *Clim. Change* **109** 33–57

Robock A 2000 Volcanic eruptions and climate *Rev. Geophys.* **38** 191–219

Robock A, Oman L and Stenchikov G L 2008 Regional climate responses to geoengineering with tropical and Arctic SO_2 injections *J. Geophys. Res.* **113** D16101

Shepherd J G 2009 *Geoengineering the Climate: Science, Governance and Uncertainty* (The Royal Society) London (https://royalsociety.org/topics-policy/publications/2009/geoengineering-climate)

Solar Radiation Management Governance Initiative 2011 *Solar Radiation Management: The Governance of Research* (The Royal Society) London (https://royalsociety.org/topics-policy/projects/solar-radiation-governance/report)

Steffen W *et al* 2018 Trajectories of the Earth system in the anthropocene *Proc. Natl Acad. Sci. USA* **115** 8252–9

Swann A L S, Hoffman F M, Koven C D and Randerson J T 2016 Plant responses to increasing CO_2 reduce estimates of climate impacts on drought severity *Proc. Natl Acad. Sci. USA* **113** 10019–24

Tilmes S, Richter J H, Mills M, Kravitz B and MacMartin D G 2018 Stratospheric Aerosol Geoengineering Large Ensemble Project - GLENS, National Center for Atmospheric Research (NCAR), (https//doi.org/10.5065/D6JH3JXX)

Tilmes S *et al* 2018 stratospheric aerosol geoengineering large ensemble project *Bull. Am. Meteorol. Soc.* **99** 2361–71

Tilmes S, Muller R and Salawitch R 2008 The sensitivity of polar ozone depletion to proposed geoengineering schemes *Science* **320** 1201–4

Tilmes S, Sanderson B M and O'Neill B C 2016 Climate impacts of geoengineering in a delayed mitigation scenario *Geophys. Res. Lett.* **43** 8222–9

Tilmes S *et al* 2013 The hydrological impact of geoengineering in the geoengineering model intercomparison project (GeoMIP) *J. Geophys. Res. Atmos.* **118** 11,036–11,058

Tjiputra J F, Grini A and Lee H 2016 Impact of idealized future stratospheric aerosol injection on the large-scale ocean and land carbon cycles *J. Geophys. Res. Biogeosci.* **121** 2–27

Townshend J R G 1992 Improved Global Data for Land Applications: A Proposal for a New High Resolution Data Set: Report of the Land Cover Working Group of IGBP-DIS IGBP Secretariat, the Royal Swedish Academy of Science p 87 (https://www.igbp.net/download/18.950c2fa1495db7081e1942/1430900178610/IGBP_report_20-Global_Data_land.pdf)

Watson R T *et al* 2000 *IPCC Special Report: Land Use, Land-Use Change, and Forestry* Cambridge University Press, London (https://www.ipcc.ch/report/land-use-land-use-change-and-forestry/)

Xia L, Robock A, Tilmes S and Neely R R III 2016 Stratospheric sulfate geoengineering could enhance the terrestrial photosynthesis rate *Atmos. Chem. Phys.* **16** 1479–89

Yoon J-H and Zeng N 2010 An Atlantic influence on Amazon rainfall *Clim. Dyn.* **34** 249–64

Yu M, Wang G and Chen H 2016 Quantifying the impacts of land surface schemes and dynamic vegetation on the model dependency of projected changes in surface energy and water budgets *J. Adv. Model. Earth Syst.* **8** 370–86